Chapter 12

Theoretical Modeling of Structural Dynamics[†]

[†]adapted from J. Tang, D.-S. Yang, A. H. Zewail, *J. Phys. Chem. C* **111**, 8957 (2007).

Introduction

The developments in ultrafast electron crystallography (UEC) have provided the means to study structural dynamics following femtosecond optical excitations. Some of the systems investigated are metallic (Ch. 11) and semiconducting (Ch. 4) materials and oriented molecules on a substrate (*1*). In these studies, a general behavior was found; namely, a large-amplitude expansion of the lattice structure on the ultrashort time scale and restructuring at longer times. Such structural dynamics were directly derived from the temporal change of the position of Bragg spots (or diffraction rings), which are often accompanied by similar temporal profiles for the diffraction intensities and widths.

The pertinent questions are several: What causes the large structural change at short times? What is the atomic-scale description of the phenomena? What determines the time scales for reaching the maximum change and for restructuring? In previous chapters, the transient lattice expansion in semiconductors was shown to be potential-driven with a critical role for phonon-induced coherent motion (Chs. 4 and 5). The time scales of hot carriers and their interactions with phonons, and the relaxation through subsequent phonon–phonon couplings, were also shown to be important in the description of the dynamics. However, a theory at the microscopic level is necessary for further investigation of the forces controlling the atomic-scale motions. Such a model may also be important for elucidation of laser-induced melting and ablation (*2-4*) and acoustic wave generation (*5-14*), and for studies involving transient optical reflectivity (*15-17*), time-resolved x-ray diffraction (*18-24*), and transmission electron diffraction of metals (*25-27*).

In this chapter, a theoretical study is presented for the investigation of the atomic forces responsible for the structural changes of substrates and adsorbates following an

optical excitation. For the simplest case, the substrate–adsorbate system can be modeled as atoms connected by harmonic oscillators in linear chains, taking into account frictional damping and the external driving force. The impulse-induced structural dynamics of this array of atoms was simulated for forces with different functional forms. The time dependence of the position of Bragg diffraction spots was systematically analyzed in order to determine the relevant controlling factors. Comparison with the experimental results was then made.

In what follows, it will be shown that, following an ultrashort impulse, a thin film (~30 nm) may exhibit cycles of oscillatory expansion and contraction that disappear in a thick substrate. Unlike the ordinary linear expansion in static, thermal equilibrium, which is incoherent and has its origin in the (local) anharmonicity of the crystal potential, the large-amplitude expansion is driven by the impulsive force, which results in a coherent, nonlocal sound wave effect. Such expansion is followed by a slow decay, cycles of periodic expansion and contraction, or both. For adsorbates, this far-from-equilibrium expansion, with some contraction at short times, is also observed. The maximum shift of a Bragg spot and the corresponding delay time are found to be dependent on the chain length of the adsorbate and on the nature of the coupling between the substrate and adsorbate.

This chapter is organized as follows: All of the relevant terms used in this work are summarized in Table 1. In the Theory Section, the model Hamiltonian and the equations of motion for the substrate and adsorbate atoms are described, together with the needed diffraction expressions of UEC. Afterward, the methodology and results of numerical simulations are presented. Discussions of the importance of different parameters and their association with real systems are provided before the conclusion.

Table 1: Nomenclature for Symbols

N (N_A)	no. of substrate (adsorbate) atoms in the 1D array
z_n (Z_n)	displacement of the nth atom in the substrate (adsorbate)
m (m_A)	mass of a substrate (adsorbate) atom
ω (ω_A)	angular frequency of the spring in the substrate (adsorbate)
ℓ (ℓ_A)	interatomic distance between substrate (adsorbate) atoms at equilibrium; lattice spacing
γ	friction coefficient; frictional damping factor for the spring oscillations
F_n (G_n)	external impulsive force on the nth atom in the substrate (adsorbate)
L	thickness of the substrate; $L \equiv (N-1)\,\ell$
Λ_F	attenuation length of the impulsive force
τ_{rise} and τ_{decay}	rise and decay time constants of the impulsive force
v_s	sound velocity in the substrate; $v_s = \ell\,\omega$
s	wavevector change (in the crystallographer's convention) of the elastically scattered electrons along the surface normal direction
$\langle \Delta s(t) \rangle$	shift of the peak position of the first-order Bragg spot
ζ_e	penetration depth of the probing electrons
τ_S, τ_A, τ_{SA}	effective time constants for heat transfer between adjacent atoms in the substrate, in the adsorbate, and across the adsorbate–substrate interface, respectively

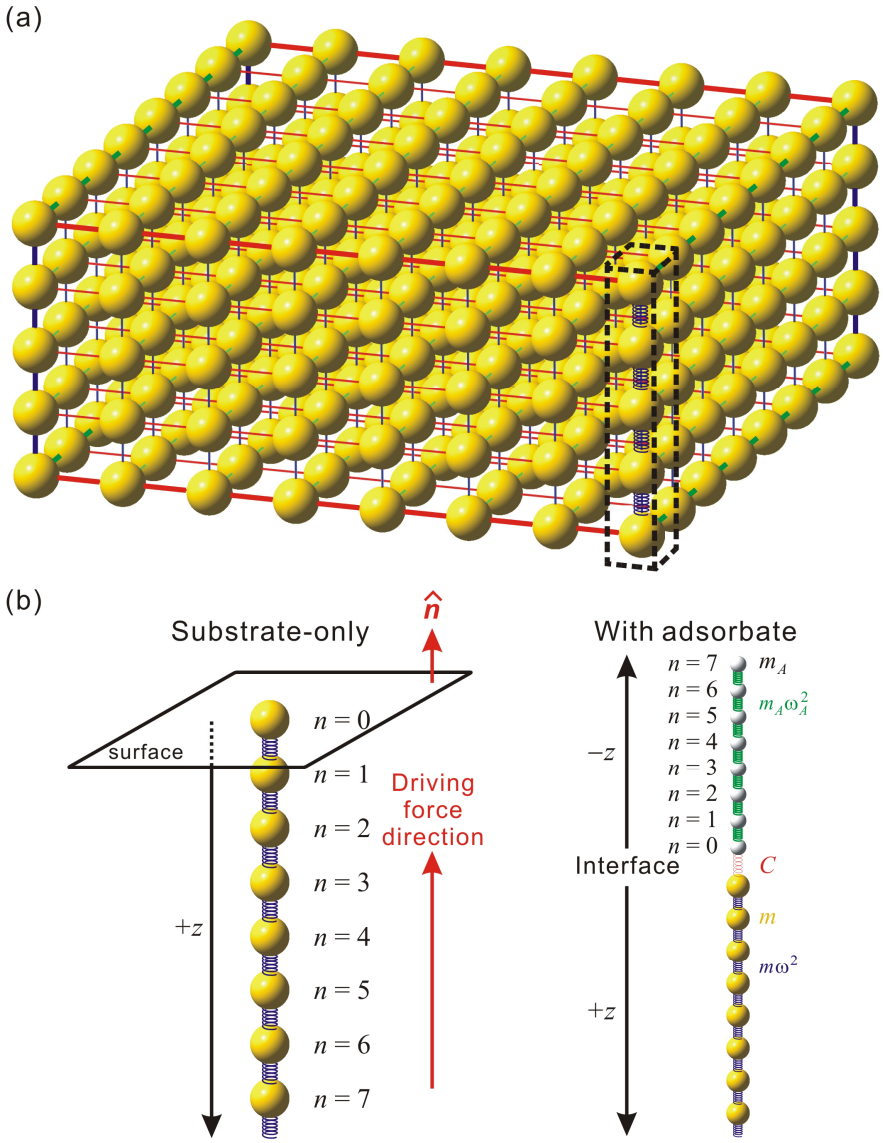

Fig. 1. Atomic picture of the substrate/adsorbate composite system. (a) A 3D simple lattice. Each lattice site is an atom that is connected to the neighboring ones by springs. The 3D lattice is further simplified as a 1D array of atoms along the surface normal direction (black dashed box) (b) The 1D atomic arrays considered in our microscopic model for only the substrate (left) and for the substrate/adsorbate composite system (right). The surface normal and driving-force directions are indicated, and the indices of atoms are shown. Masses of the substrate and adsorbate atoms and the force constants for different bondings are labeled with the corresponding colors.

Theory: Microscopic Models and Structural Dynamics

Here, a simple lattice consisting of arrays of atoms connected by springs is considered (Fig. 1). Due to the stress constraints of the surface and the geometry of the laser-excited region, lattice expansion occurs mainly along the surface normal direction. In the expansion-restricted, two-dimensional (2D) horizontal directions on the surface, hundreds of micrometers to a few millimeters (relatively uniform with a low excitation gradient) are covered, whereas the lattice under the excitation of only nanometer-to-micrometer penetration into the bulk (high excitation gradient) is free to expand along the surface normal direction (Ch. 4). Thus, the 3D lattice (Fig. 1a) can be further simplified as spring-connected atoms in a 1D chain, and such simplification should not be of major consequence in the description of dynamical phenomena on the time scale of interest. The same consideration can also be applied to the modeling of adsorbates on a substrate (Fig. 1b). In the following section, we first consider this microscopic model for the substrate and derive the analytical solutions for the atomic motions under the influence of impulsive force; manifestations of such dynamics in the UEC patterns will be deduced. The microscopic model for adsorbate molecules on the substrate will then be provided.

A. Substrates

The substrate atoms, each with a mass, m, are coupled to their nearest neighbors through harmonic springs with a force constant $m\omega^2$, where ω is the angular frequency. Due to the aforementioned excitation geometry, the external force, induced by a femtosecond laser pulse, is taken to be parallel to the z axis (the chain axis), and it causes atomic motions along this direction. Therefore, the Hamiltonian for a chain of N atoms is given by

$H_S = \sum_{n=0}^{N-1} \frac{p_n^2}{2m} + \frac{m\omega^2}{2} \sum_{n=0}^{N-2} (z_n - z_{n+1})^2$; the atoms are indexed from $n = 0$ to N–1, and p and z are the momentum and displacement, respectively. [See Appendix A for the application of the more general Fermi–Pasta–Ulam model (*28*), which contains an anharmonic cubic term in the Hamiltonian.]

If the vibrational motion is damped by a frictional force and the nth atom is subject to an external impulsive force, $F_n(t)$, the equations of motion for such a system are given by

$$\begin{aligned}
&\frac{d^2}{dt^2} z_0 + \gamma \frac{d}{dt} z_0 + \omega^2 (z_0 - z_1) = \frac{F_0(t)}{m}, \\
&\frac{d^2}{dt^2} z_n + \gamma \frac{d}{dt} z_n + \omega^2 (2z_n - z_{n-1} - z_{n+1}) = \frac{F_n(t)}{m}, \quad (n = 1, 2, \cdots, N-2) \\
&\frac{d^2}{dt^2} z_{N-1} + \gamma \frac{d}{dt} z_{N-1} + \omega^2 (-z_{N-2} + z_{N-1}) = \frac{F_{N-1}(t)}{m},
\end{aligned} \tag{1}$$

where γ is a friction parameter; here, we loosely term a friction coefficient. With the initial condition at time zero for the nth atom (defining $\dot{z}_n(0)$ and $z_n(0)$ as the velocity and displacement at time $t = 0$), Eq. 1 can be solved analytically (see Appendix B for details). The closed-form solution is

$$\begin{aligned}
z_n(t) = &\frac{1}{N} \sum_{j=0}^{N-1} \left[z_j(0) + \dot{z}_j(0) \frac{1 - e^{-\gamma t}}{\gamma} + \frac{1}{M} \int_0^t d\tau \, F_j(\tau) \frac{1 - e^{-\gamma (t-\tau)}}{\gamma} \right] \\
&+ \frac{2}{N} \sum_{k=1}^{N-1} \sum_{j=0}^{N-1} \cos\left(\frac{\pi k}{N} \left(n + \frac{1}{2} \right) \right) \cos\left(\frac{\pi k}{N} \left(j + \frac{1}{2} \right) \right) \times \\
&\left[\begin{array}{l} z_j(0) e^{-\frac{\gamma t}{2}} \left(\cos(\Lambda_k t) + \frac{\gamma \sin(\Lambda_k t)}{2\Lambda_k} \right) + \dot{z}_j(0) e^{-\frac{\gamma t}{2}} \frac{\sin(\Lambda_k t)}{\Lambda_k} \\ \\ + \frac{1}{m} \int_0^t d\tau \, F_j(\tau) e^{-\frac{\gamma (t-\tau)}{2}} \frac{\sin(\Lambda_k (t-\tau))}{\Lambda_k} \end{array} \right],
\end{aligned} \tag{2}$$

where $M \equiv Nm$, $\Lambda_k = \Omega_k \sqrt{1 - \left(\gamma^2 / 4\Omega_k^2\right)}$ for the kth normal mode, and $\Omega_k = 2\omega \sin(\pi k/2N)$, which is the angular frequency if friction is absent. The first sum in Eq. 2 describes the motion for the center of mass of the chain. It can be omitted if the concern is only for the relative motions between atoms. The remaining part in Eq. 2 describes the motion of each atom and, therefore, is relevant to the observations made by diffraction methods; the intensity and position of a Bragg diffraction spot depend on the relative atomic distances but not on the absolute position of the center of mass.

The index k (from 1 to N–1) enumerates the normal modes in the atomic chain. Accordingly, two eigenvalues, λ_{1k} and $\lambda_{2k} = -\gamma/2 \pm i\Lambda_k$, are found for each vibrational mode; their appearance in the exponents determines the type of atomic motions that may be seen. If the friction coefficient, γ, is small (the underdamped regime), $i\Lambda_k$ is a pure imaginary number which leads to an oscillatory motion, $\exp(i\Lambda_k)$. Because of the dependence of Ω_k on the wavevector (defined as $\pi k/N\ell$, where ℓ is the lattice spacing), this dispersion relation indicates that wave propagation may be expected, and the slope near zero wavevector gives the speed of sound. In contrast, if γ is much greater than $\Omega_k/2$ (the overdamped regime), $i\Lambda_k$ becomes a real number, and nonoscillatory damped motions are to be expected in the array of atoms.

The regimes of underdamped (coherent) and overdamped (diffusive) atomic motions can be seen in the form of Eq. 1 in the continuum limit. The present harmonic model for a discrete lattice array can be simplified in the limit of a small ℓ, relative to the spatial profile of the impulsive force. The discrete rate equation for each site can then be approximated by a differential equation involving a continuous position variable, z. With the definitions of total elastic modulus, $K \equiv m\omega^2/(N-1)$, and total length $L \equiv (N-1)\ell$,

Eq. 1 reduces in the continuum limit to

$$\frac{\partial^2}{\partial t^2} q(z,t) + \gamma \frac{\partial}{\partial t} q(z,t) - \frac{K L^2}{M} \frac{\partial^2}{\partial z^2} q(z,t) = \frac{F(z,t)}{M}, \tag{3}$$

where $q(z, t)$ is the vibrational amplitude at position z and time t, and $F(z, t)/M$ is the force per unit mass. In the absence of friction, that is, when $\gamma = 0$, Eq. 3 becomes

$$\frac{\partial^2}{\partial t^2} q(z,t) - \frac{K L^2}{M} \frac{\partial^2}{\partial z^2} q(z,t) = \frac{F(z,t)}{M}, \tag{4}$$

which resembles the inhomogeneous 1D wave equation with a propagation speed (sound velocity) $v_s \equiv L \sqrt{K/M} = \ell\, \omega$. Note that this value is exactly the slope of the aforementioned dispersion relation (Ω_k vs $\pi k / N\ell$) near zero wavevector: $[\mathrm{d}\Omega_k/\mathrm{d}(\pi k/N\ell)]_{k\to 0} = \ell\, \omega$.

On the other hand, in the overdamped regime with $\gamma \gg \omega$, and for $t \gg \gamma/\omega^2$, Eq. 3 can be approximated by

$$\frac{\partial}{\partial t} q(z,t) - \frac{K L^2}{M \gamma} \frac{\partial^2}{\partial z^2} q(z,t) = \frac{F(z,t)}{M \gamma}, \tag{5}$$

which is in the form of a 1D diffusion equation with a diffusion constant $D \equiv KL^2/M\gamma = \omega^2 \ell^2/\gamma = \ell^2/\tau_D$, where τ_D, or γ/ω^2, is the diffusion correlation time. Thus, the more general Eq. 3 bridges two extremes, the wave equation of Eq. 4 and the diffusion equation of Eq. 5, with each regime representing one type of atomic motion.

B. Observables in UEC

On the basis of the aforementioned model, the position of the nth atom along the chain direction (which is opposite to the surface normal) is $n\ell + z_n(t)$, where $z_n(t)$ is its time-dependent displacement from the equilibrium position. Given such a geometry at time t, the amplitude $A(\vec{s},t)$ of the elastically scattered electrons, with the momentum transfer $\hbar \cdot 2\pi \vec{s}$ being parallel to the surface normal, is the Fourier transform (*29*) of the potential U_n of the nuclei and electrons in the s domain,

$$A(\vec{s},t) = \sum_{n=0}^{N-1} \int d^3 r_n \; U_n(\vec{r}_n)\, e^{i2\pi \vec{s}\cdot\vec{r}_n} \; e^{i2\pi|\vec{s}|(n\ell + z_n(t))} \\ = \sum_{n=0}^{N-1} e^{i2\pi|\vec{s}|(n\ell + z_n(t))}\, \overline{U}_n(\vec{s}), \tag{6}$$

where $\overline{U}_n(\vec{s}) \equiv \int d^3 r_n \, U_n(\vec{r}_n)\, e^{i2\pi\vec{s}\cdot\vec{r}_n}$; the wavevector, $\vec{s}$, is defined here using the crystallographer's convention. The atomic scattering factor, $\overline{U}_n(\vec{s})$, for electron diffraction for the *n*th atom may be approximated by a Gaussian function of the wavevector $s \equiv |\vec{s}|$, expressed as $\exp(-\pi^2 s^2 / 2\sigma_{S,n}^2)$, with the Debye–Waller factor included. The subscript S stands for substrate. For an array of *N* identical atoms, $\overline{U}_n(\vec{s})$ is independent of the site index *n*, and the normalized diffraction intensity, $I_S(s, t)/I_0$ (relative to the direct beam intensity I_0), for a given *s* becomes

$$\frac{I_S(s,t)}{I_0} = \left|\frac{A(\vec{s},t)}{N}\right|^2 = \left|\frac{1}{N}\sum_{n=0}^{N-1} \exp\left[-\pi^2 s^2 / 2\sigma_S^2 + i2\pi s\left(n\ell + z_n(t)\right)\right]\right|^2. \tag{7}$$

For all simulations presented in this study, $\sigma_S \ell = 5$ is used so that higher-order Bragg spots are attenuated when compared with the first-order one.

Because of the periodicity of the lattice, $I_S(s, t)$ exhibits a sinc-function dependence on *s* whenever $s\ell$ is close to an integer. If there are no atomic displacements, that is, $z_n(t) = 0$ for all lattice sites, the *j*th Bragg spot will peak at $s = j/\ell$. If all *N* atoms are assumed to contribute to the Bragg diffraction, the first moment of $I_S(s, t)$ (i.e., the peak shift of the Bragg diffraction, $\langle \Delta s(t) \rangle_S$) for the first Bragg spot at $s \sim 1/\ell$ can be calculated using

$$\left\langle \Delta s(t) \right\rangle_S \equiv \frac{\int_{s_1}^{s_2} ds \; s\, I_S(s,t)}{\int_{s_1}^{s_2} ds \; I_S(s,t)} - \frac{1}{\ell}, \tag{8}$$

where $s_1 = (1 - 1/N)/\ell$ and $s_2 = (1 + 1/N)/\ell$ correspond to the edges of the central Bragg peak near $1/\ell$; the width of the central dominant lobe of $I_S(s, t)$ is inversely proportional to $N\ell$. It follows that information about lattice dynamics can be obtained by monitoring $\langle \Delta s(t) \rangle_S$, the deviation of the average peak position at time t.

Due to the large kinetic energy of the probing electrons used in UEC, low-order Bragg diffraction can only be observed at a grazing incidence angle. In such a reflection geometry, because of the large electron–material scattering cross section and the small penetration depth of the incident electrons, a smaller number of (fewer layers of) atoms N_B near the surface contribute to the Bragg diffraction substantially. Therefore, N in Eqs. 7 and 8 needs to be replaced by N_B in order to take this attenuation effect into account; or more precisely, if ζ_e ($\zeta_e/N\ell \ll 1$) is the penetration depth of the electron beam, Eq. 7 can be replaced by

$$\frac{I_S(s,t)}{I_0} = \left| \frac{1}{N} \sum_{n=0}^{N-1} \exp\left[-\pi^2 s^2 / 2\sigma_S^2 + i 2\pi s \left(n\ell + z_n(t) \right) - n\ell / \zeta_e \right] \right|^2 . \qquad (9)$$

The lower and upper bounds for the integration in Eq. 8 accordingly change to $s_1 = 1/\ell - 1/\zeta_e$ and $s_2 = 1/\ell + 1/\zeta_e$.

C. Adsorbates

So far, only the substrate has been considered. The above harmonic model for a substrate slab can be further extended to include chainlike molecules oriented on the substrate surface. We shall consider two connected chains along a 1D line, with the bottom region representing the substrate and the top the adsorbate, as illustrated in Fig. 1b. The total Hamiltonian H is then given by

$$
\begin{aligned}
H &= H_{\mathrm{S}} + H_{\mathrm{A}} + H_{\mathrm{AS}}\,, \\
H_{\mathrm{S}} &= \sum_{n=0}^{N-1} \frac{p_n^2}{2m} + \frac{m\omega^2}{2} \sum_{n=0}^{N-2} \left(z_n - z_{n+1}\right)^2, \\
H_{\mathrm{A}} &= \sum_{n=0}^{N_{\mathrm{A}}-1} \frac{P_n^2}{2m_{\mathrm{A}}} + \frac{m_{\mathrm{A}}\,\omega_{\mathrm{A}}^2}{2} \sum_{n=0}^{N_A-2} \left(Z_n - Z_{n+1}\right)^2, \\
H_{\mathrm{SA}} &= \frac{C}{2}\left(z_0 - Z_0\right)^2,
\end{aligned}
\tag{10}
$$

where H_{S} is the Hamiltonian for the substrate, H_{A} describes a monolayer of chainlike adsorbates with N_{A} atoms (each has a mass m_{A}, and the spring constant is $m_{\mathrm{A}}\omega_{\mathrm{A}}{}^2$), and H_{SA} describes the coupling; the subscript A stands for adsorbate. The lower-case letters p and z denote the momentum and displacement for a substrate atom, and the capital letters P and Z, for an atom of the adsorbate molecule. The equations of motion according to such a Hamiltonian, with additional frictional force and external impulsive force $F_n(t)$ on the nth substrate atom and $G_n(t)$ on the nth adsorbate atom, can be written as

$$
\begin{aligned}
\frac{d}{dt} z_n &= \frac{p_n}{m} \quad (n = 0, \ldots, N-1) \\
\frac{d}{dt} Z_n &= \frac{P_n}{m_{\mathrm{A}}} \quad (n = 0, \ldots, N_{\mathrm{A}} - 1)
\end{aligned}
\tag{11}
$$

and

$$
\begin{aligned}
\frac{d}{dt} p_0 &= F_0(t) - \gamma\, p_0 - m\omega^2 (z_0 - z_1) - C(z_0 - Z_0) \\
\frac{d}{dt} p_n &= F_n(t) - \gamma\, p_n - m\omega^2 (2z_n - z_{n-1} - z_{n+1}) \quad (n = 1, \ldots, N-2) \\
\frac{d}{dt} p_{N-1} &= F_{N-1}(t) - \gamma\, p_{N-1} - m\omega^2 (z_{N-1} - z_{N-2}) \\
\frac{d}{dt} P_0 &= G_0(t) - \gamma_A\, P_0 - m_A\omega_A^2 (Z_0 - Z_1) - C(Z_0 - z_0) \\
\frac{d}{dt} P_n &= G_n(t) - \gamma_A\, P_n - m_A\omega_A^2 (2Z_n - Z_{n-1} - Z_{n+1}) \quad (n = 1, \ldots, N_A - 2) \\
\frac{d}{dt} P_{N_A-1} &= G_{N_A-1}(t) - \gamma_A\, P_{N_A-1} - m_A\omega_A^2 (Z_{N_A-1} - Z_{N_A-2}).
\end{aligned}
\tag{12}
$$

Similar to the structural dynamics of the adsorbate, the normalized diffraction intensity $I_A(s, t)$ for an N_A-unit chainlike molecule is given by

$$\frac{I_A(s,t)}{I_0} = \left| \frac{1}{N_A} \sum_{n=0}^{N_A-1} \exp\left[-\pi^2 s^2 / 2\sigma_A^2 + i 2\pi s \left(-n \ell_A + Z_n(t) \right) \right] \right|^2, \tag{13}$$

where the negative sign for the phase $2\pi s(-n \ell_A)$ from the nth atom is due to our convention of indexing adsorbate atoms on the $-z$ axis and substrate ones on the $+z$. For the first-order Bragg spot, $\langle \Delta s(t) \rangle_A$ is given by

$$\left\langle \Delta s(t) \right\rangle_A \equiv \frac{\int_{s_1}^{s_2} ds\, s\, I_A(s,t)}{\int_{s_1}^{s_2} ds\, I_A(s,t)} - \frac{1}{\ell_A}, \tag{14}$$

where $s_1 = (1 - 1/N_A)/\ell_A$ and $s_2 = (1 + 1/N_A)/\ell_A$.

Numerical Simulations and Results

A. Methodology: The Substrate

To understand the manifestations of dynamical changes of the substrate lattice structure in diffraction, we shall calculate $z_n(t)$ using the analytical solution of Eq. 2 or the numerical solution of Eq. A2, followed by the computation of $\langle \Delta s(t) \rangle_S$ using Eq. 8. It is therefore necessary to specify the temporal and spatial profiles of the driving force, $F_n(t)$, in order to proceed with the calculations. For simplicity, this impulsive force is assumed to extend spatially into the substrate slab with an exponential attenuation, that is, $F_n(t) = F_0(t) \cdot \exp(-n \ell / \Lambda_F)$, where Λ_F is the attenuation length.

The temporal profile of the stress impulse $F_0(t)$ can take a pulse shape such as a Gaussian or a stretched exponential function. For the former case, $F_0(t) = -|F_0| \cdot \exp(-(t-\tau_0)^2/2\tau_p^2)$, where τ_0 is the delay time and τ_p is the duration of the impulse;

the negative sign of F_0 is due to the convention of placing the lattice sites on the $+z$ axis and therefore the laser-induced expansion impulse being along the $-z$ direction. For the latter case, we consider the stretched exponential function in the form of $f(t/\tau) \equiv \exp(-\sqrt{t/\tau})$, and the temporal stress profile to be $F_0(t) = -|F_0|\cdot[-f(t/\tau_{\text{rise}})+f(t/\tau_{\text{decay}})]/[-f(\tau_{\max}/\tau_{\text{rise}})+f(\tau_{\max}/\tau_{\text{decay}})]$; such a profile with a decay time τ_{decay} longer than the rise time τ_{rise} (i.e., $0 < \tau_{\text{rise}} < \tau_{\text{decay}}$) reaches its maximum amplitude at $t = \tau_{\max}$, where $\sqrt{\tau_{\max}} = \ln\sqrt{\tau_{\text{decay}}/\tau_{\text{rise}}} \Big/ \left(\sqrt{\tau_{\text{rise}}^{-1}} - \sqrt{\tau_{\text{decay}}^{-1}}\right)$. Compared to the Gaussian profile, the stretched exponential form has a longer trailing tail, which may represent better the actual stress caused by the change of crystal potential, lattice temperature in the substrate, or both; that is, the impulse represents an "induced force" or "temperature jump" rather than the ultrashort laser pulse itself. The physical meanings of the rise and decay time constants will be addressed in the Discussion Section.

Another type of temporal profile for the impulsive force may originate from a diffusion-controlled mechanism such as carrier diffusion, heat conduction, or both. In this case, the long-time decay of the impulse follows a temporal dependence of $1/\sqrt{t}$. To take into account the rise of the impulse and the diffusion-type decay at longer times, we can have the temporal impulse profile expressed as

$$F_0(t) = -|F_0|\cdot[(1 - \exp(-t/\tau_{\text{rise}}))(1 + \tau_{\max}/\tau_{\text{decay}})^{1/2}]/[(1 - \exp(-\tau_{\max}/\tau_{\text{rise}}))(1 + t/\tau_{\text{decay}})^{1/2}]$$

with $0 < \tau_{\text{rise}} < \tau_{\text{decay}}$, where $\tau_{\max} \equiv \tau_{\text{rise}}\cdot\ln(3 + 2\,\tau_{\text{decay}}/\tau_{\text{rise}})$ is the time for $|F_0(t)|$ to reach its maximum. Following such an impulse profile, it will be shown that the temporal evolution of $\langle\Delta s(t)\rangle_S$, when displayed on a logarithmic scale in time, reflects the simple dependence of $1/\sqrt{t}$ at longer times, which has been observed experimentally (Ch. 4).

The parameters deduced from the properties of gold are used for the following

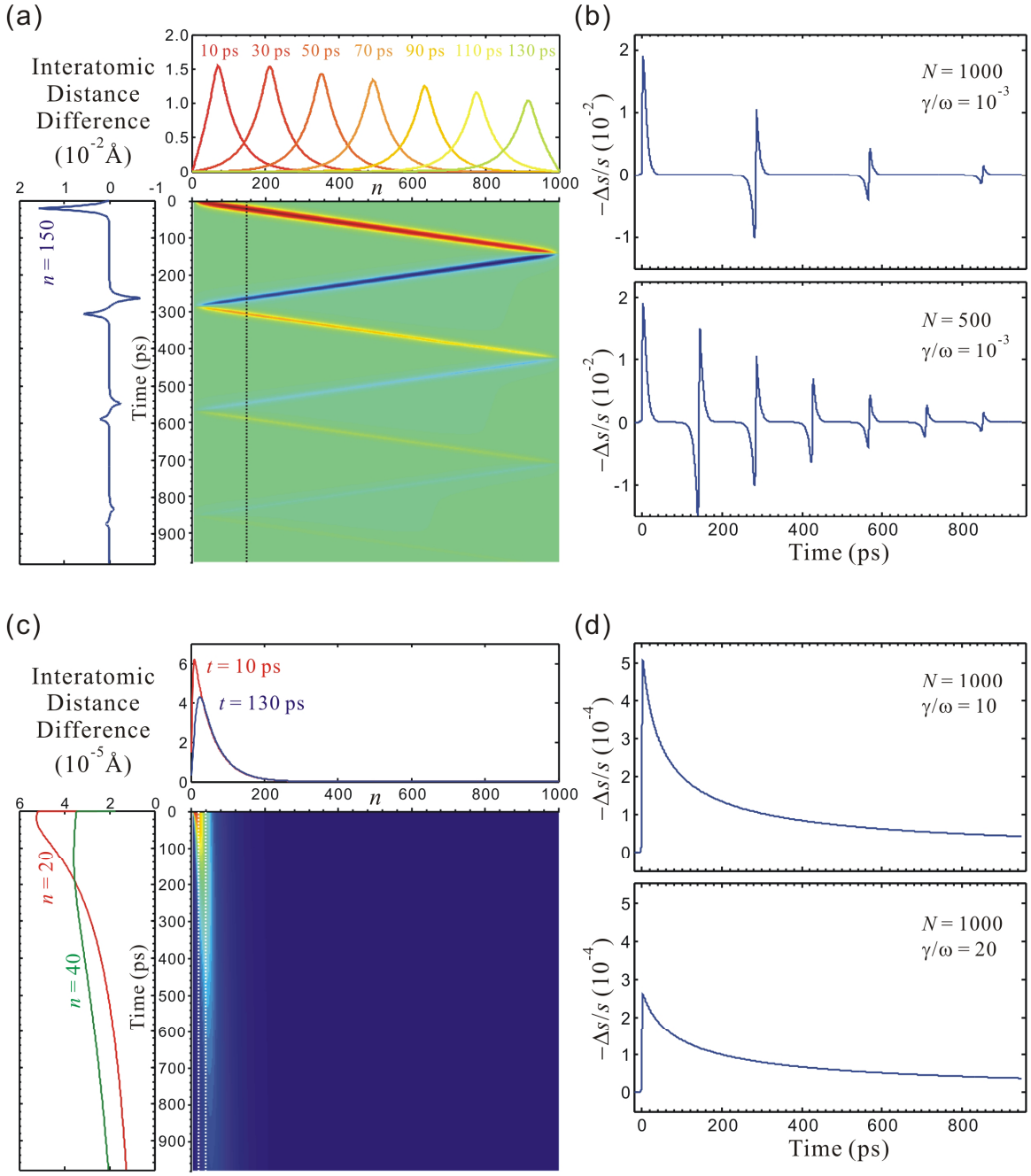

(See next page for the figure caption.)

Fig. 2. Substrate structural dynamics. Both the underdamped and overdamped regimes are considered in the time domain and diffraction space. The external force has a temporal profile of the stretched exponential functional form with $\tau_{\text{rise}} = \tau_{\text{decay}} = 1$ ps, an attenuation length $\Lambda_{\text{F}} = 50\,\ell$, and a maximum value $|F_0| = 10^{-11}$ N; $N = 1000$. (a) The underdamped regime with $\gamma/\omega = 10^{-3}$. The temporal and spatial dependence of the interatomic distance change, $z_n(t) - z_{n-1}(t)$, is shown in a 2D plot. The zigzag pattern clearly shows the nature of wave propagation for lattice deformation in the slab; the upper panel shows the lattice deformation at selected times and illustrates the wave propagation phenomenon. The waveform travels at the speed of sound (2030 m/s), which is evident from the time (~280 ps) when the wave returns to the surface (i.e., the round-trip traveling time). The left panel shows the temporal dependence of the interatomic distance change at a given site $n = 150$. (b) Temporal dependence of the relative change in the peak position of the first-order Bragg spot, $-\Delta s/s$; the electron probing depth $\zeta_{\text{e}} = 10\,\ell$ covers the lattice changes near the surface only. A positive (negative) diffraction change refers to expansion (contraction) of the lattice in the surface region. Manifestation of the propagation of the lattice deformation waveform can be found from the recurrence of diffraction changes (upper); the recurrence period is reduced by half if the slab thickness is halved (lower). The decay of the signal is due to the frictional damping. (c) The overdamped regime with $\gamma/\omega = 10$. Compared to the 2D plot in panel a, the fast wave propagation (the zigzag pattern) disappears and is replaced by much slower temporal evolution of lattice changes. Note that the change of interatomic distances is more than 2 orders of magnitude smaller than those in panel a. In addition, due to the strong frictional damping, the changes are rather limited within the top of the slab (upper panel), and their slow time scale can be seen more clearly in the left panel. (d) $-\Delta s/s$ vs time. The diffraction change is much smaller than that in panel b, and its temporal evolution is slow (upper). With a larger friction coefficient, the diffraction change becomes even smaller and is on an even longer time scale (lower).

numerical simulations. First, the propagation velocity v_s (= $\ell\,\omega$ in the continuum and friction-free limit) is presumed to be equal to the experimentally measured sound velocity of 2030 m/s for the extensional mode (*30*). With ℓ being equal to the smallest spacing between atoms in crystalline gold (2.88 Å), we obtain $\omega = 7.05\times10^{12}$ rad/s, or $\nu = \omega/2\pi = 37$ cm^{-1}. Each gold atom has a mass of $m = 3.27\times10^{-25}$ kg, which therefore leads to a force constant of $m\omega^2 = 16.3$ N/m. As for the consideration of a moderate driving force, $|F_0|$ is chosen to be 10^{-11} N. We use $\zeta_e/\ell = 10$ to take into account the finite penetration depth of the probing electrons in the substrate. For the structural dynamics probed by UEC, the substrate is at its thermal equilibrium prior to the laser excitation; thus, for simplicity, the initial velocities and atomic displacements from the equilibrium positions are all taken to be 0 at negative times.

B. Substrate Structural Dynamics

To illustrate the different atomic motions in the underdamped and overdamped regimes, we plot in Fig. 2 the results of numerical simulations for $z_n(t)$ and the corresponding diffraction spot shift $\langle\Delta s(t)\rangle_S$ using the same parameters and external force (stretched exponential function for the temporal profile), except for the value of γ. It is clear that in the underdamped regime, wave propagation inside the slab and reflection at the boundaries are the dominant features of the atomic motions (the zigzag pattern in Fig. 2a); the value of the friction coefficient determines the rate of the waveform damping at longer times. For a slab of $N = 1000$, the traveling time required for a round trip is ~280 ps, and it is reduced by half if the slab thickness is halved (Fig. 2b). Upon the return of the waveform to the surface, a contraction is seen first and closely followed by the expansion; this lattice contraction exists because the returning expansion waveform compresses the surface lattice from underneath before it is reflected at the free boundary

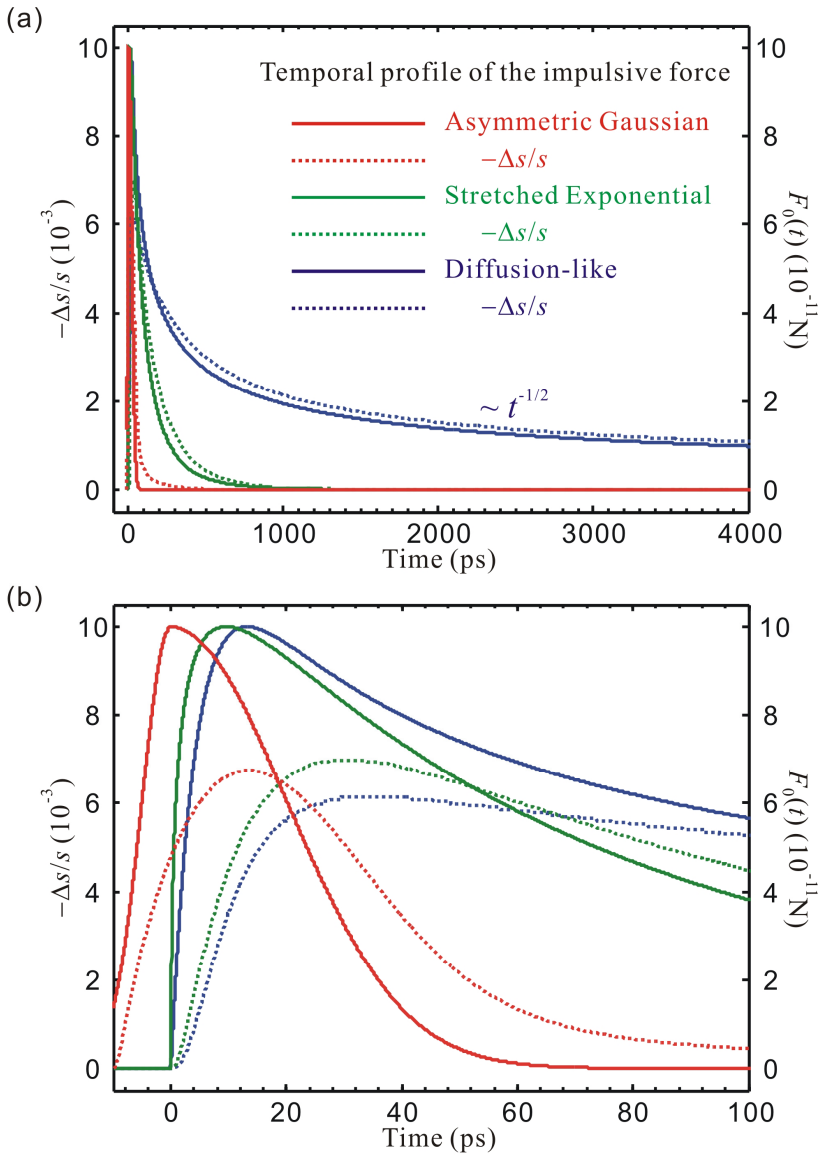

Fig. 3. Effect of force profile on diffraction change with time. Different temporal force profiles $F_0(t)$ and the corresponding diffraction changes, $-\Delta s/s$, are shown on (a) longer and (b) shorter time scales. The common parameters are $N = 1000$, $\gamma/\omega = 10^{-2}$, $|F_0| = 10^{-11}$ N, $\Lambda_F = 500\,\ell$, $\tau_{rise} = 5$ ps, $\tau_{decay} = 20$ ps, and $\zeta_e = 10\,\ell$. (a) On a longer time scale, $-\Delta s/s$ resembles $F_0(t)$; for the external force with a diffusion-like temporal dependence ($\sim t^{-1/2}$), the corresponding diffraction change also exhibits a similar behavior. (b) For a given $|F_0|$, the maximum change in $-\Delta s/s$ is similar, and its appearance time follows the peak of the impulse profile.

and leads to the surface expansion. It is noted that broadening of the traveling lattice deformation is minor due to the long-wave propagation (a width of ~50 ℓ) considered here.

In contrast, the diffusive nature of the atomic motions is seen in the overdamped regimes (Fig. 2c); not many features can be observed from the structural dynamics, except for the diffusion-type slow decay after an initial rise (Fig. 2d). A larger γ leads to a smaller diffraction spot shift initially. At a first glance, the temporal behavior of the decay seems to resemble the experimentally observed dynamics, but the very small magnitude of spot shift (at least an order of magnitude less than that in the underdamped regime) does not match with our experimental observations of large lattice expansions. In addition, the physical properties of crystalline materials negate the large-friction scenario: the phenomenon of sound wave propagation always exists in ordered solids. It is noted that, according to Eq. 5 with a given D, the diffusion time scale for a distance of electron probing ($\zeta_e = 10\ \ell$), which governs the decay of the $\langle \Delta s(t) \rangle_S$ signal, becomes $(\zeta_e/\ \ell\ )^2\ \tau_D = (\zeta_e/\ \ell\ )^2(\gamma\ /\omega^2) = 14.2\ (\gamma\ /\omega)$ ps (Fig. 2d, on the order of hundreds of picoseconds). A large γ might probably occur in a system that is extremely highly excited (large electronic and lattice interaction), or is not ordered, with numerous low-frequency local degrees of freedom that define the friction. However, neither of these scenarios is within the consideration of our model. Thus, the overdamped regime as a proper description of the structural dynamics can be ruled out. In what follows, we shall only consider the underdamped regime; typically, $\gamma/\omega = 10^{-2}$.

Figure 3 presents the influence of the functional form of the temporal force profile $F_0(t)$ on the diffraction change $\langle \Delta s(t) \rangle_S$; the calculations were performed using the same parameters except for the different forms described in the previous subsection. It is

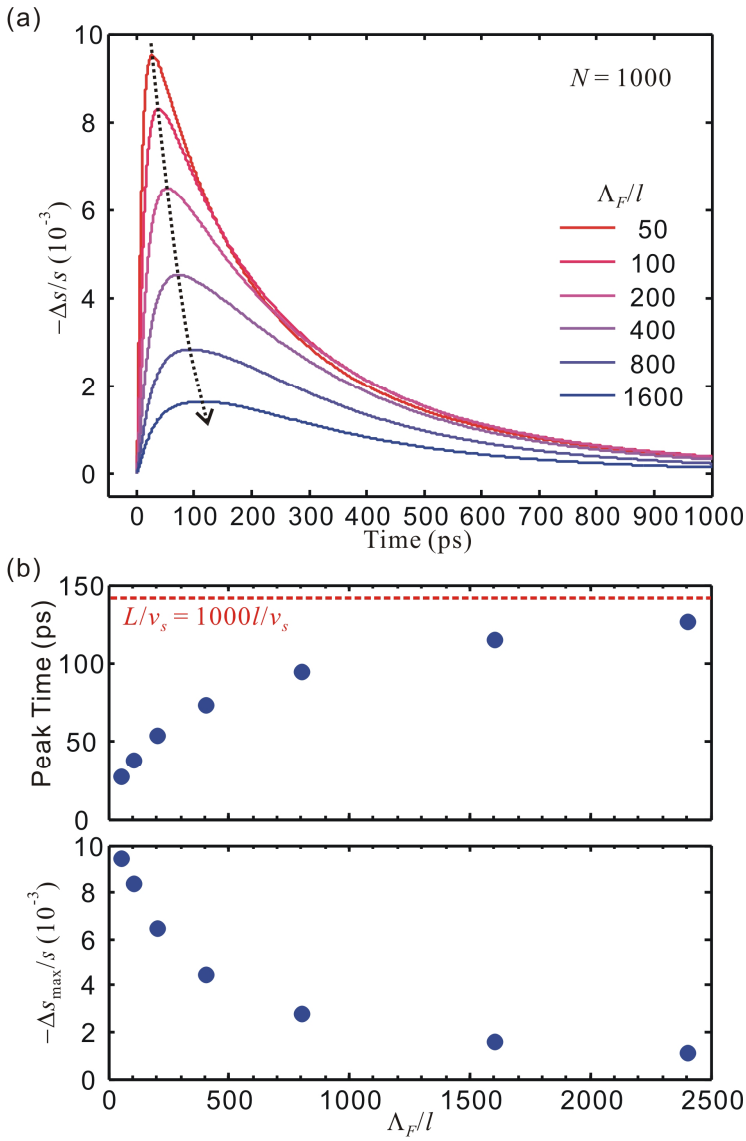

Fig. 4. Effect of the spatial attenuation length of the impulse force on diffraction changes. (a) The driving force has a temporal profile of the stretched exponential functional form with $\tau_{\text{rise}} = 5$ ps and $\tau_{\text{decay}} = 50$ ps; $|F_0| = 10^{-11}$ N, $N = 1000$ and $\gamma/\omega = 10^{-2}$. As the impulsive force extends deeper into the bulk (larger Λ_F), the maximum of $-\Delta s/s$ decreases and appears at a later time. The decay of $-\Delta s/s$ in the cases of small Λ_F is more apparent. (b) The dependence of the peak delay time (upper panel) and maximum diffraction change (lower panel) on Λ_F. The asymptotic value L/v_s in the upper panel has its origin in the propagation's being wavelike in nature.

noticeable that the features of wave propagation/reflection and recurring contraction/expansion disappear, which will be further examined later. The purpose of this figure is to show that the external driving force determines the overall shape of the diffraction transient; the faster the force decays, the sooner the diffraction change disappears. In other words, from the experimentally observed diffraction changes, the knowledge about the impulsive force in an optically excited material can be obtained. Another interesting observation is that for a given value of $|F_0|$ (10^{-11} N here), the maximum change in $\langle \Delta s(t) \rangle_S$ seems to be less affected by the temporal difference in $F_0(t)$, although its appearance time closely follows the impulse profile.

In order to elucidate the effect of the penetration of the impulsive force, we use the same temporal profile of the stretched exponential function and the same parameters (N, γ, etc.) but vary the attenuation length, Λ_F, of the force in the simulations. Figure 4a shows that as Λ_F becomes larger, the maximum diffraction spot shift diminishes and appears at a later time; the decay of the transient change is much apparent in the cases of small Λ_F. The latter observation may be connected with the experimentally observed fast decays. Figure 4b shows the dependence of the peak time and maximum spot shift on Λ_F. The trends may be understood according to the following arguments. A larger attenuation length means less difference between the driving forces on neighboring atoms, which results in a smaller lattice expansion and, consequently, a smaller diffraction spot shift (Fig. 4b, lower panel). Moreover, as Λ_F becomes comparable to the slab thickness, substantial driving force exists not only at the surface but also within the slab, even at the other end. As a result, the lattice deformation originated from the bulk will propagate toward the surface at the speed of sound, and the interference between different contributions shifts the peak time of $\langle \Delta s(t) \rangle_S$. The asymptotic value L/v_s clearly indicates

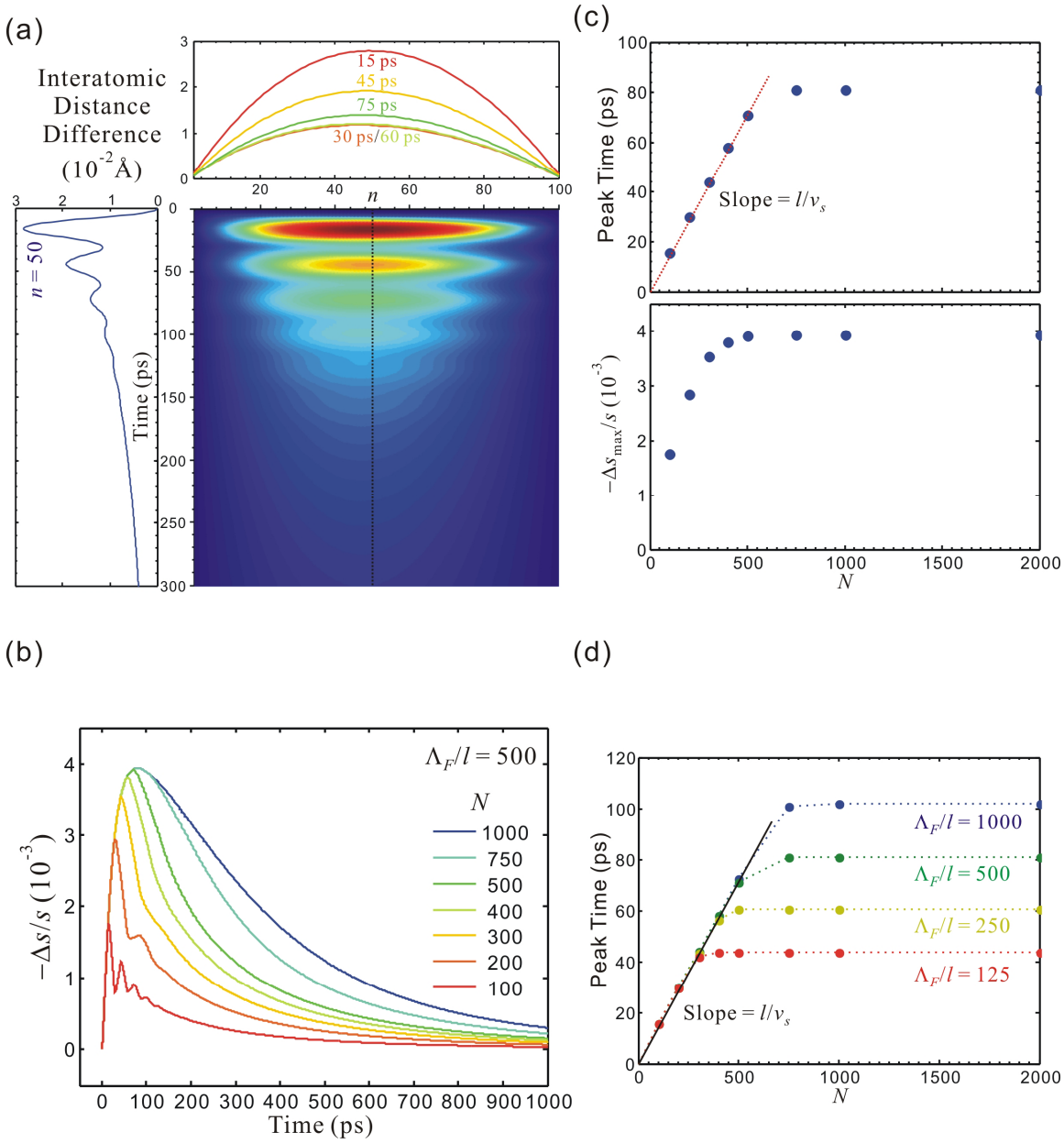

(See next page for the figure caption.)

Fig. 5. Effect of the slab thickness on structural dynamics and diffraction changes. The driving force has the same temporal profile and maximum value as in Fig. 4, and $\gamma/\omega = 10^{-2}$. (a) Temporal and spatial dependence of the interatomic distance changes in a 2D plot; $N = 100$ and $\Lambda_F = 100\,\ell$. In such a thin slab, the whole substrate exhibits a coherent breathing motion (a standing wave, as evident in the upper panel), and the oscillation period is the same as the round-trip traveling time (28.4 ps) for wave propagation. The slab center has the largest lattice deformation, whose temporal evolution is shown in the left panel. (b) Temporal evolution of $-\Delta s/s$ with different N; $\Lambda_F = 500\,\ell$ is kept the same. It is clear that the coherent breathing motion is only apparent in a thin substrate; as the slab thickness increases (for $N < \Lambda_F/\ell$), such a breathing motion disappears, but both the maximum diffraction change and its appearance delay time increase. However, further increase in N, beyond Λ_F/ℓ, does not affect the increase in the diffraction change at early times. These phenomena are the combined results of the wave propagation and the frictional damping in the lattice in the underdamped regime. (c) Dependence of the peak delay time (upper panel) and maximum diffraction change (lower panel) on N from the results in panel b. The linear increase in the peak delay time is the evidence of the wavelike propagation in the system; the peak delay time is equal to $N\ell/v_s = L/v_s$ (half of the round-trip traveling time). (d) The N-dependence shown in the upper plot of panel c is general, even for different values of Λ_F.

the nature of wave propagation in the lattice (Fig. 4b, upper panel).

Through the comparison between Figures 2b and 4a, the reason for the disappearance of the apparent oscillatory behavior in $\langle \Delta s(t) \rangle_S$ becomes clear. In a thick substrate slab, the larger friction constantly diminishes the lattice deformation and makes its return to the surface insignificant. In addition, as the rise and decay time constants of the driving force become larger, the $\langle \Delta s(t) \rangle_S$ signal follows and may cover the recurring components. However, the phenomenon of wave propagation still exists in these cases, since it is intrinsic in the underdamped regime.

Figure 5 presents, with Λ_F and other parameters being fixed, the dependence of the structural dynamics and diffraction change on the slab thickness. Interestingly, in a thinner slab of $N = 100$ ($L = 28.8$ nm), a coherent breathing motion (a standing wave) for the whole substrate is found, and the oscillation period is the same as the round-trip traveling time (28.4 ps) for wave propagation (Fig. 5a). The coherent motion is the result of the interference between the lattice deformation components generated at different parts of the substrate. In fact, Fig. 5a is not very different from Fig. 2a: the decrease of the substrate thickness reduces the round-trip traveling time, and the increase in the time constants of the impulse spatially broadens the width of lattice deformation (the horizontal axis in the figures) and temporally induces an average effect of the deformation amplitude (the vertical axis in the figures). It is noted that in such a system, the surface expands the least, and the atoms near the middle of the slab actually experience the largest increase in interatomic spacings. At longer times, the frictional force and the decay of the impulsive force dictate the decrease of the lattice expansion.

The aforementioned coherent motion disappears as the substrate thickness increases (Fig. 5b). This result is therefore expected because of the increase in the wave

traveling time (which means less temporal average effect; the vertical axis in Fig. 5a) and the weaker interference by the lattice deformation from the deeper part of the substrate (the dissipation of structural changes due to the frictional force). Thus, for a given Λ_F, the maximum diffraction spot shift increases and occurs at a later time as N becomes greater (but still remains smaller than Λ_F/ℓ). When the dependence on N is plotted (Fig. 5c), the linear increase in the peak time (upper panel, $N < \Lambda_F/\ell$) indicates once again the nature of wave propagation in the underdamped regime; the saturation phenomenon can also be understood because a further increase in N beyond Λ_F/ℓ only brings in limited additional contribution of the lattice changes and hence will not affect the structural dynamics near the surface. By changing Λ_F, such a relationship of the substrate thickness still remains valid, as demonstrated in Fig. 5d.

C. Methodology: The Adsorbate

As shown in Subsection C of the Theory Section, the adsorbate assembly is treated similar to that of the substrate slab, provided that they are separately considered. However, because of the coupling between the two (H_{SA} of Eq. 10), further considerations of how to determine the temporal and spatial profiles of the impulsive forces over both the substrate and adsorbate are required. Here, instead of assuming different force profiles of $F_n(t)$ and $G_n(t)$ for the substrate and adsorbate separately, we consider the following model. Initially, the excitation laser pulse is only absorbed by the substrate and causes a temperature jump. Because of the spatial temperature gradient and energy transfer, the adsorbate acquires a temperature increase from the heated substrate. By considering the energy transport in the substrate/adsorbate composite system, the induced lattice strains (driving forces) can be formulated, and we can simulate the structural responses (z_n and Z_n) and, consequently, the diffraction changes ($\langle \Delta s \rangle_S$ and

$\langle \Delta s \rangle_{\mathrm{A}}$), which correspond to structural dynamics of the substrate and adsorbate over time.

With the substrate temperature, T_n, at the nth lattice site and the adsorbate temperature, Y_n, at the nth atom, temperature changes can be expressed in the following equations describing the energy flow in terms of temperature gradients:

$$\begin{aligned}
&\frac{d}{dt}T_0 = S_0(t) - \frac{1}{\tau_{\mathrm{S}}}(T_0 - T_1) - \frac{1}{\tau_{\mathrm{SA}}}(T_0 - Y_0),\\
&\frac{d}{dt}T_n = S_n(t) - \frac{1}{\tau_{\mathrm{S}}}(2T_n - T_{n-1} - T_{n+1}) \qquad (n = 1,\ldots, N-2),\\
&\frac{d}{dt}T_{N-1} = S_{N-1}(t) - \frac{1}{\tau_{\mathrm{S}}}(T_{N-1} - T_{N-2}),\\
&\frac{d}{dt}Y_0 = -\frac{1}{\tau_{\mathrm{A}}}(Y_0 - Y_1) - \frac{1}{\tau_{\mathrm{SA}}}(Y_0 - T_0),\\
&\frac{d}{dt}Y_n = -\frac{1}{\tau_{\mathrm{A}}}(2Y_n - Y_{n-1} - Y_{n+1}) \qquad (n = 1,\ldots, N_{\mathrm{A}} - 2),\\
&\frac{d}{dt}Y_{N_{\mathrm{A}}-1} = -\frac{1}{\tau_{\mathrm{A}}}(Y_{N_A-1} - Y_{N_A-2}).
\end{aligned} \tag{15}$$

The second and fifth equations in the group indicate that these temperatures at different sites are governed by a heat transfer process. Since the energy content at a certain site is equal to the temperature within a constant factor, the left-hand side of Eq. 15, which is proportional to the time derivative of the energy content, is proportional (without an external heat source) to the net difference between the incoming and outgoing energy fluxes which are linearly associated with the energy (temperature) gradients. This difference in temperature gradients gives the right-hand side of Eq. 15 a second-order, spatial, finite difference of temperatures for the nonboundary atomic sites in the case of a discrete lattice.

In Eq. 15, τ_{S}, τ_{A} and τ_{SA} are the effective time constants of energy transfer between adjacent atoms in the substrate, in the adsorbate, and at the interface, respectively; they originate from the combination of lattice spacings, thermal conductivities, and heat capacities for the substrate and adsorbate. These time constants

are treated as parameters and may not necessarily correspond to the actual values in the thermally equilibrated diffusion regime. The external source $S_n(t)$ represents the absorbed heat which in this case is the laser heating pulse; it has the following temporal and spatial dependences invoked:

$$S_n(t) = S_0(t)\, e^{-\frac{n\ell}{\zeta_{\text{laser}}}} = \sqrt{\frac{4\ln 2}{\pi}}\,\frac{S_0}{\tau_{\text{p}}}\, e^{-4\ln 2\left(\frac{t-\tau_0}{\tau_{\text{p}}}\right)^2} e^{-\frac{n\ell}{\zeta_{\text{laser}}}}, \tag{16}$$

where ζ_{laser} is the penetration depth of the laser in the substrate. We use $\zeta_{\text{laser}} = 16.3$ nm for the gold substrate and the full-width-at-half-maximum (fwhm) of the laser pulse to be 200 fs.

The impulsive force is assumed to linearly depend on the temperature change; that is, $F_n(t) = const \times T_n(t)$ and $G_n(t) = const \times Y_n(t)$ where *const* is a proportionality constant related to the Grüneisen parameter γ_{lat} of the material. This linear relationship originates from the following equations: the longitudinal stress impulse $\delta\sigma_{33} = -\gamma_{\text{lat}} C_{\text{lat}} \delta T$ where C_{lat} is the specific heat per unit volume (*5, 8*), and the total force impulse (over an area of square unit cell length) $F = \ell^2\, \delta\sigma_{33}$. Therefore, with $\gamma_{\text{lat}} \sim 3$ and $C_{\text{lat}} = 2.5\times10^6$ J/(m^3·K) for gold (*8*), *const* is about 6.2×10^{-13} N/K. In the present study, *const* is assumed to be 10^{-12} N/K for both the substrate and adsorbate for simplicity. Therefore, after the temperatures, $T_n(t)$ and $Y_n(t)$ with both the spatial and temporal evolution, are obtained by solving Eq. 15, we obtain $F_n(t)$ and $G_n(t)$, which can then be substituted into Eqs. 11 and 12 for the calculation of $z_n(t)$ and $Z_n(t)$.

For the UEC investigation of the substrate/adsorbate composite system, we need to consider the underdamped regime, and for this purpose, we consider the damping factor $\gamma/\omega = 0.01$ for the substrate and $\gamma_{\text{A}}/\omega_{\text{A}} = 0.1$ for the adsorbate. A larger adsorbate friction coefficient is used because the assembly of chainlike molecules often has a less

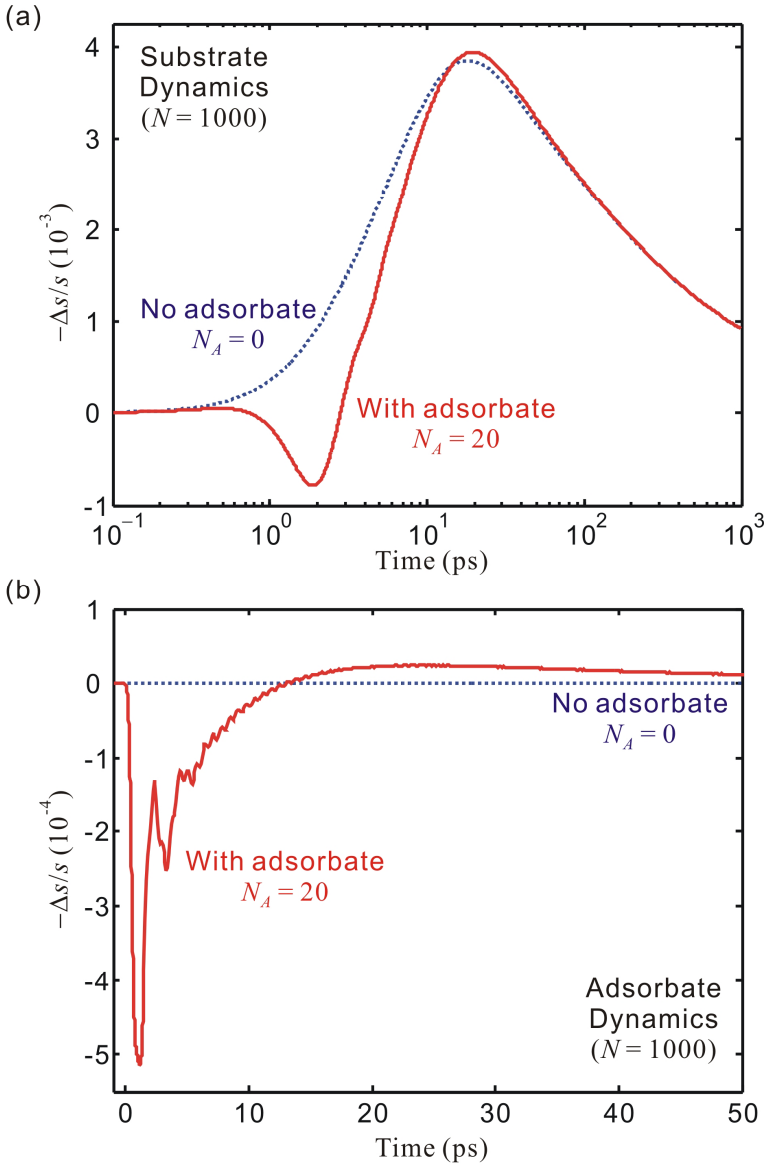

Fig. 6. Substrate and adsorbate dynamics, in the absence of coupling. Diffraction changes from (a) the substrate and (b) the adsorbate without direct energy transfer across the interface are shown. (a) The substrate dynamics in the presence of the adsorbate (red solid line) and with no adsorbate (blue dashed line). Although the long-time dynamics is less affected, the existence of the adsorbate causes a small contraction in the surface region of the substrate at early time, followed by a lattice expansion on a time scale of ~10 ps. Note that the time axis is a logarithmic scale. (b) The adsorbate dynamics (red solid line). Due to the expansion movement of the substrate, the adsorbate mostly shows contraction; the many oscillations are the results of wave propagation and frictional damping in the adsorbate and the interference between the substrate and adsorbate motions.

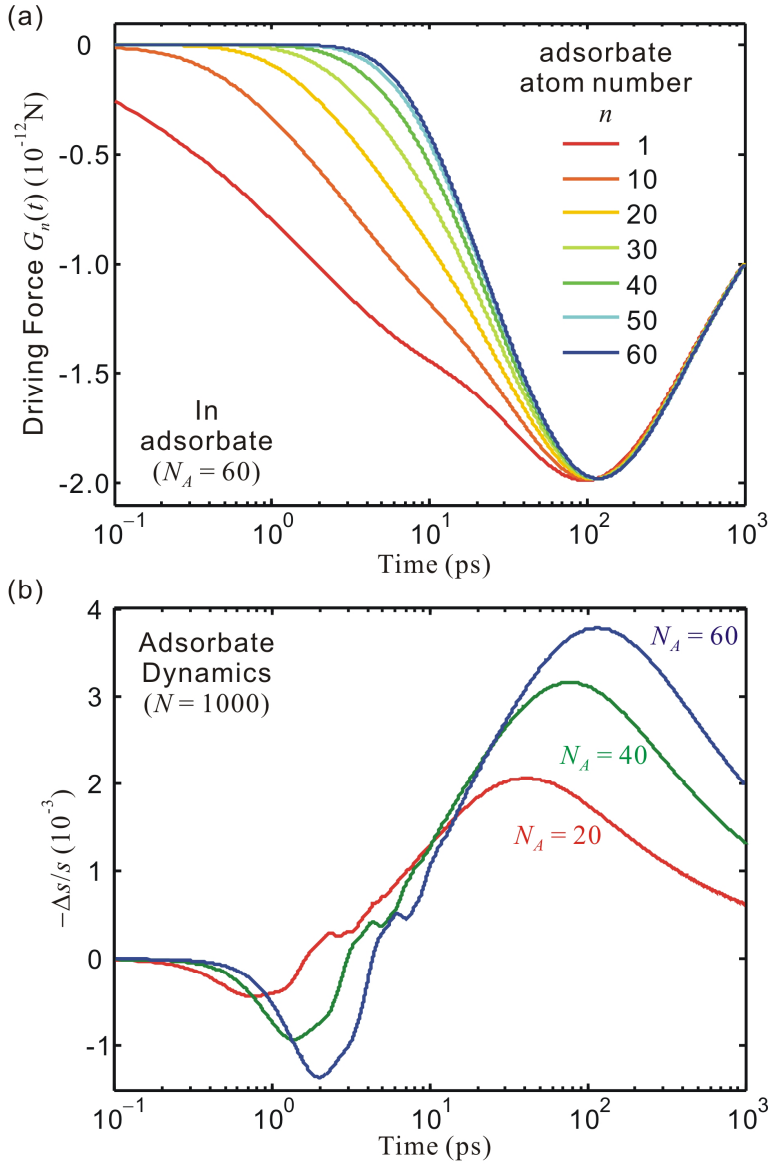

Fig. 7. Substrate and adsorbate structural dynamics in the presence of coupling. Adsorbate atom driving force and the effect of adsorbate length, $N_A \ell_A$, on dynamics are shown. Here, for the simulation of heat transfer in the substrate/adsorbate composite system, $\tau_S = \tau_A = 0.01$ ps and $\tau_{SA} = 1$ ps are used (see text for details about other parameters). (a) The delay in the onset of change in the external driving force reflects the speed of heat transfer across the interface. In tens of picoseconds, the entire adsorbate of the molecular system acquires the new temperature. (b) The adsorbate dynamics shows a small contraction in the molecular structure at a very early time, followed by expansion in tens of picoseconds and restructuring on an even longer time scale. As N_A increases, a clearer contraction and larger expansion are obtained; the maximum expansion/contraction also appears at a later time.

ordered structure, and frictional motions are, in general, more frequent. The force constants used for the substrate, adsorbate, and the interfacial spring are 16.3, 50, and 5 N/m, respectively. The relative magnitudes of these force constant values are to reflect the strength of different bondings in the composite system. The time constant, τ_S, is assumed to be 0.01 ps to reflect the fast energy conduction (through ballistic carrier transport) in gold, and τ_A and τ_{SA} for the adsorbate and the interfacial junction are variables.

D. Adsorbate Structural Dynamics

Let us first consider the structural dynamics of both the substrate and the adsorbate under the condition of no substantial energy transport across the interface. In this case, the external impulsive force is exclusively applied to only the substrate atoms, and the adsorbate atoms, with one end connected to the substrate, are governed by the (underdamped) oscillators. In Fig. 6, the calculated $\langle \Delta s(t) \rangle_S$ and $\langle \Delta s(t) \rangle_A$ show that, because of the existence of an unexcited adsorbate molecule above the substrate, the initial expansion of the underlying substrate atoms in the adsorbate direction leads to a transient contraction near the substrate surface at very short time; the long-time behavior is relatively unaffected (Fig. 6a). In contrast, the adsorbate mostly shows contraction due to the expansion movement of the substrate (Fig. 6b). It follows from the simulations that, without energy coupling across the interface, the adsorbate will show only contraction in the interatomic spacings, contrary to the lattice expansion observed experimentally.

If the energy transfer across the interface is switched on, a different temporal behavior in the adsorbate dynamics arises. We first examine the temporal and spatial evolution of the temperature (which is also the impulsive force by a constant factor) in the adsorbate (Fig. 7a). The rate of the amplitude increases at the interface ($n = 0$) is

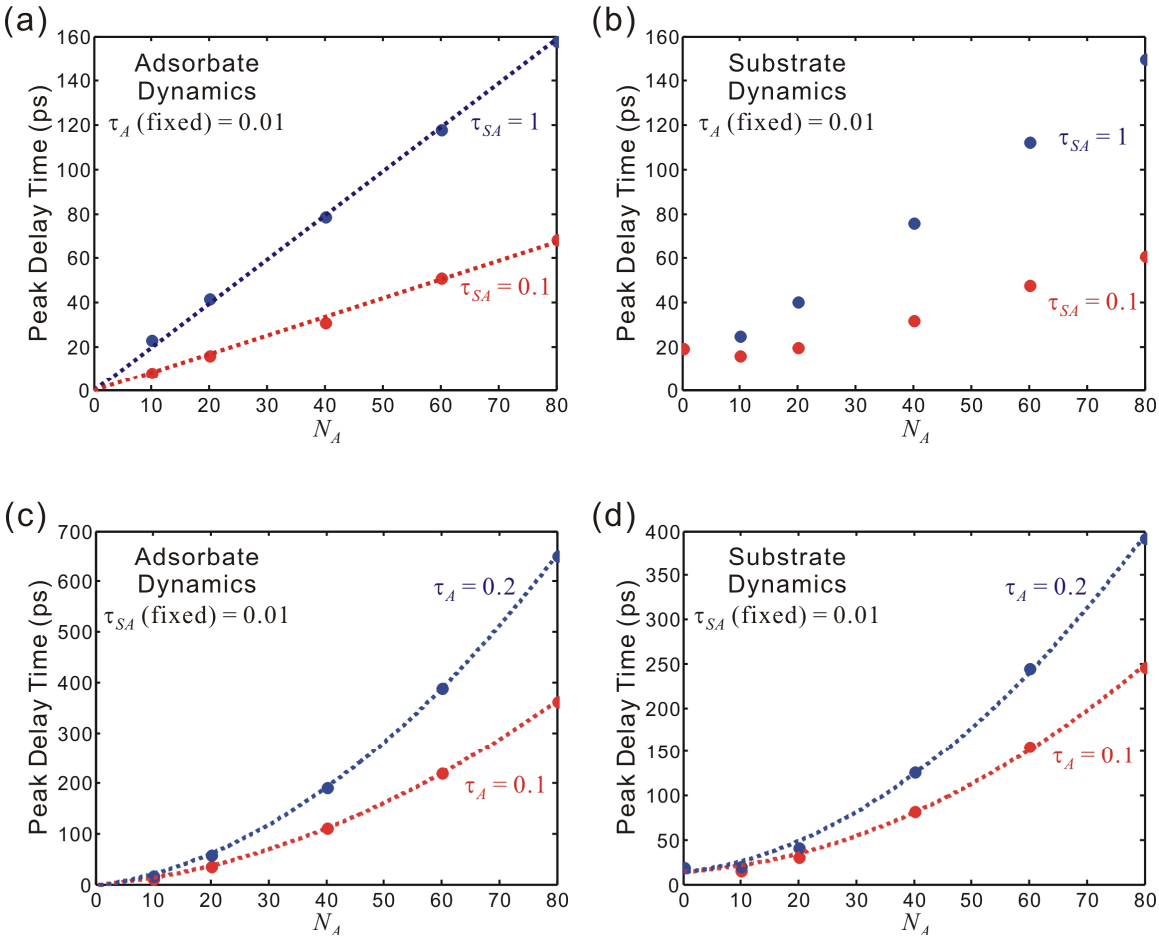

Fig. 8. Adsorbate dynamics dependence on transfer time. Dependence of the peak delay times of diffraction changes $-\langle \Delta s(t) \rangle_A / s$ and $-\langle \Delta s(t) \rangle_S / s$ on N_A with selected values of τ_{SA} and τ_A is shown. (a) When τ_{SA} is much larger than τ_A, the peak delay time of the adsorbate dynamics appears to be linearly dependent on N_A. (b) The peak delay time of the substrate dynamics also becomes larger as the adsorbate molecule becomes longer; in the cases of short adsorbate molecules, interference between the adsorbate and substrate motions may shift the peak delay time of the substrate dynamics to a smaller value. (c and d) When τ_{SA} is fixed and much smaller than τ_A, the peak delay times of the adsorbate and substrate dynamics appear to be quadratic with N_A. This dependence is a consequence of 1D heat diffusion along the adsorbate chain; τ_A becomes the dominant controlling factor for the heat transfer.

naturally controlled by τ_{SA}, and the delay time in the onset of change for atoms farther away from the interface is governed by τ_A. After equilibration of the adsorbate molecule is reached, the impulse at different atoms decays homogeneously at a rate determined again by τ_{SA}.

Figure 7b presents the temporal evolution of the diffraction change for different lengths of the adsorbate molecule. Because of the energy transfer to the adsorbate, the contraction-only dynamics in Fig. 6b is modified with the inclusion of structural expansion and recovery over a longer time scale. The maximum change in $\langle \Delta s(t) \rangle_A$ and its corresponding time increase with adsorbate length; this is reminiscent of a similar trend observed in Fig. 5b. Hence, the previous arguments about lattice deformation propagation and the interference between structural changes generated at different atoms can be applied here for the understanding of Fig. 7b.

The adsorbate/substrate (A/S) dynamics can be further categorized into the (A/S) coupling-controlled and (A) heat-transfer-controlled regimes. If τ_{SA} is appreciably longer than τ_S and τ_A, one can expect the thermal coupling at the interface to be the bottleneck of the energy transfer: a longer τ_{SA} leads to further delay in the peak of $\langle \Delta s(t) \rangle_{A/S}$ (Fig. 8, panels a and b). It is reasonable to see that, for a given τ_{SA}, the peak time is in a linear relationship with N_A, because the deterministic step occurs at the interface and an additional adsorbate length only linearly shifts the time at which maximum structural changes are reached. This is the coupling-controlled regime. In contrast, if τ_A is larger or comparable to τ_{SA}, the diffusion process in the adsorbate becomes the dominant factor for the structural dynamics. As a result, the peak time of $\langle \Delta s(t) \rangle_{A/S}$ shows a quadratic dependence on N_A ($\sim (N_A \ell_A)^2/D_{eff}$ where $D_{eff} = \ell_A^2/\tau_A$), a consequence of 1D heat diffusion along the adsorbate chain (Fig. 8, panels c and d). This is the heat-transfer-

controlled scenario. It is natural that for the same N_A, a larger τ_A makes the peak time appear at a later time.

It is noted that the peak time of $\langle \Delta s(t) \rangle_A$ is unaffected if the adsorbate force constant, $m_A \omega_A^2$, or the coupling force constant, C, in Eq. 12 is doubled. Thus, the rise of a diffraction spot shift is, indeed, determined by the induced thermal impulse, which is solely controlled by those heat-transfer correlation time constants. It is interesting to see that the size of the adsorbate molecules can influence the magnitude and peak time of $\langle \Delta s(t) \rangle_S$. Such an effect is mainly contributed by the adsorbate structural dynamics on the substrate surface layers where the diffraction is measured.

Discussion and Conclusion

As presented in the numerical results and figures, the important variables in the present microscopic model can be categorized into the following four: (1) the underdamped vs overdamped regime, which is determined by the relative magnitudes of the friction coefficient γ and the vibrational angular frequency ω; (2) the functional form for the temporal profile of the impulsive force, $F_0(t)$; (3) the substrate thickness, $N\ell$, and the attenuation length, Λ_F, for the impulse spatial profile F_n; and (4) the adsorbate effect, that is, the dependence of structural dynamics on the adsorbate chain length $N_A \ell$ and on the time scales of energy transport within the adsorbate and across the interface. We have concluded that the underdamped regime is appropriate for the UEC observations studied. This conclusion directly supports the wave-propagating structural changes of the lattice, which plays a key role in the phenomena of coherent lattice motions and interferences in structural deformation.

Structural dynamics closely follows the temporal evolution of $F_0(t)$. With a

moderate driving force, the lattice may have up to a few percent changes in the interatomic spacings, resulting in a clear diffraction spot shift. This observation is fundamentally significant in that the observed lattice expansion deduced from the Bragg spot movement is not necessarily linked to conventional thermal expansions due to a temperature rise. In fact, it has been experimentally shown that the picture of thermal equilibrium cannot account for ultrafast structural dynamics (Ch. 4). However, using the simple microscopic model with an external driving force, we are able to obtain the calculated temporal behavior of the diffraction spot shift, which is similar to the experimental observations. Such a model is useful in relating UEC experimental results to motions of individual atoms and to the forces exerted.

The three different types of functional forms for $F_0(t)$ may each correspond to a certain condition in a specific type of materials. First, a Gaussian impulse profile with a full width at half maximum close to the excitation pulse width may be suitable for the discussion of the structural dynamics of metals following low-energy and low-fluence optical excitation. It is generally known that in such a condition, the electrons and lattice of a metal may reach an equilibrium on a sub-picosecond to picosecond time scale (*31*), which implies the legitimacy of translating the electronic excitation impulse into an impulsive force in the lattice. In contrast, if the carriers and lattice do not equilibrate on a sub-picosecond time scale, which is common in a semiconductor because of the involvement of optical phonons (Ch. 4) and possibly in a highly excited metal, a stretched exponential function may be better suited for describing the rise and decay of the impulsive force. For such a case, τ_{rise} and τ_{decay} are important parameters and their values may provide additional information about the electronic and lattice dynamics in the excited material. The third type of impulse, governed by a diffusive-type process, may

also seem appropriate for many systems in which carrier or heat diffusion is involved. If an experiment shows that the spot shift follows the $1/\sqrt{t}$ relation at longer times, it may be a good indication that a diffusion-controlled impulse is at play.

By changing the two length variables, the substrate thickness $N\ell$ (i.e., the number of substrate atoms N) and the impulse attenuation length, Λ_F, different structural dynamics in the lattice can be seen, as shown in Figs. 4 and 5. A coherent lattice motion was obtained when both N and Λ_F are small (on the order of a few to tens of nanometers) and comparable. Here, the characteristic of wave propagation in the lattice system is the key. The coherent motion becomes less distinct due to a larger substrate thickness and the existence of the friction. From Fig. 5, panels b and c, it is also understood that an experimentally observed slow spot shift may not be interpreted as the result of a slow growth in the driving force; the delay in the peak time may very likely originate from the collective motion of the thicker substrate lattice.

These N- and Λ_F-dependence investigations suggest experimental thickness-dependent studies on different materials, such as crystalline metals and semiconductors, using UEC. According to the present study, we expect to observe the dependence of the time and amplitude for the maximum diffraction spot shift with metal thickness, whereas such dependence may be absent in the case of semiconductors for the following reasons. Laser excitation of metals first induces hot electrons near the surface, which permeate the whole substrate slab quickly due to their high mobility. Therefore, the induced impulsive force is likely to have an attenuation length greater than the slab thickness, and the results in Fig. 5 can be tested. In the case of semiconductors, they typically have smaller thermal conductivity and lower carrier mobility, and the generation and decay of different types of phonons may not be described well by the present model; the deterministic factors for

the peak time of $\langle \Delta s(t) \rangle_S$ have been identified experimentally (Ch. 4).

For the adsorbate effect, the simplest case of energy transfer was considered to simulate the impulsive force, although other types of force forms may be developed. However, the calculations well demonstrated the corresponding structural dynamics in the adsorbate under the variation of three important control parameters: the number of adsorbate atoms N_A, and the effective heat-transfer time constants τ_{SA} and τ_A. In short, a larger maximum diffraction spot shift will be found at a later delay time if the adsorbate molecule is longer. The coupling-controlled and heat-transfer-controlled regimes for the structural dynamics were observed, and they are governed by the relative magnitude of τ_{SA} and τ_A.

Finally, it is important to point out one of the major differences between the current impulsive force approach and the conventional heating picture. According to the latter model, as we increase the length of adsorbate molecules, oriented on the same substrate with the same interaction strength at the interface, and for the same substrate excitation fluence, the total temperature jump will decrease in the adsorbate. This is expected because of the increase in total heat capacity. Hence, as the chains becomes longer, smaller expansion of the interatomic spacings is expected. The experimental observations (*1*) are in contrast with such a prediction, and instead, they agree with the results of the present study, which indicate an increase in expansion as the chain length increases. Therefore, the nonthermal nature of ultrafast structural dynamics requires consideration of atomic motions and the forces involved. The theoretical treatment presented here can be further extended to semiconductors and other materials and for different types of forces and structures depending on the experiments of concern in UEC and related studies.

Appendix A. The Fermi–Pasta–Ulam Model

The Fermi–Pasta–Ulam Hamiltonian (*28*) with an anharmonic cubic term is

$$H = \sum_{n=0}^{N-1} \frac{p_n^2}{2m} + \frac{m\omega^2}{2} \sum_{n=0}^{N-2} (z_n - z_{n+1})^2 + \frac{\alpha\, m\omega^2}{3} \sum_{n=0}^{N-2} (z_n - z_{n+1})^3, \tag{A1}$$

where α is the anharmonicity factor (*32*) that is associated with the static linear thermal expansion coefficient β by $\beta = \alpha\, k_B\, (m\omega^2\, \ell)^{-1}$. For gold, with the spring force constant $m\omega^2 = 16.3$ N/m, $\ell = 2.88$ Å and $\beta \sim 1.4\times10^{-5}$ K^{-1}, α is $\sim 4.8\times10^{9}$ m^{-1}. Such a value makes the anharmonic term insignificant if compared with the harmonic term: for the structural changes on the order of a few percent or less, namely, $z_n - z_{n-1}$ of about a few picometers, $\alpha\ (z_n - z_{n-1}) \ll 1$. Thus, in general, one can neglect the factor α in the simulation of lattice dynamics. For the application of a very large laser fluence such that $|\Delta s/s| \sim 0.1$ but below the damage threshold (and therefore, $z_n - z_{n-1}$ is on the order of a few tenths of an angstrom), the consideration of the anharmonic cubic term leads to the following equations of motion:

$$\begin{aligned}
&\frac{d}{dt} z_n = \frac{p_n}{m} \quad (n = 1, \ldots, N) \\
&\frac{d}{dt} p_0 = F_0(t) - \gamma\, p_0 - m\omega^2 (z_0 - z_1)\left[1 + \alpha (z_0 - z_1)\right] \\
&\frac{d}{dt} p_n = F_n(t) - \gamma\, p_n - m\omega^2 (2z_n - z_{n-1} - z_{n+1})\left[1 + \alpha (z_{n-1} - z_{n+1})\right] \quad (n = 1, \ldots, N-2) \\
&\frac{d}{dt} p_{N-1} = F_{N-1}(t) - \gamma\, p_{N-1} - m\omega^2 (z_{N-1} - z_{N-2})\left[1 + \alpha (z_{N-2} - z_{N-1})\right].
\end{aligned} \tag{A2}$$

The sixth-order Runge–Kutta method can be used to obtain a numerical solution to the above equations, provided that $F_n(t)$'s are calculated from the two-temperature model or specified using a simple functional form.

Appendix B. Derivation of Equation 2

Equation 1 can be expressed in a matrix form as

$$\frac{d^2}{dt^2}\boldsymbol{z} + \gamma\frac{d}{dt}\boldsymbol{z} + \omega^2\boldsymbol{A}\boldsymbol{z} = \frac{\boldsymbol{F}(t)}{m}, \tag{B1}$$

where $\boldsymbol{z}$ is a column vector of the atomic displacements (z_0, z_1, z_2, …, z_{N-1}) and $\boldsymbol{F}$ is that of the impulsive force components (F_0, F_1, F_2, …, F_{N-1}). The matrix elements of the N-by-N matrix $\boldsymbol{A}$ are given by $\boldsymbol{A}_{ij} = 2\delta_{i,j} - \delta_{i,j+1} - \delta_{i+1,j}$ for $1 \le i, j \le N-2$ and by $\boldsymbol{A}_{0j} = \delta_{0,j} - \delta_{1,j}$ and $\boldsymbol{A}_{i,N-1} = \delta_{i,N-1} - \delta_{i+1,N-1}$; $\delta_{i,j}$ is the Kronecker delta function. With the use of the Laplace transform, Eq. B1 is turned into

$$\begin{aligned}\bar{\boldsymbol{z}}(s) = {} & \frac{1}{s^2 + \gamma s + \omega^2\boldsymbol{A}} \cdot \frac{\bar{\boldsymbol{F}}(s)}{m} \\ & + \frac{s+\gamma}{s^2 + \gamma s + \omega^2\boldsymbol{A}} \cdot \boldsymbol{z}(0) + \frac{1}{s^2 + \gamma s + \omega^2\boldsymbol{A}} \cdot \dot{\boldsymbol{z}}(0),\end{aligned} \tag{B2}$$

where $\bar{\boldsymbol{z}}(s)$ and $\bar{\boldsymbol{F}}(s)$ are the Laplace transformation of $\boldsymbol{z}(t)$ and $\boldsymbol{F}(t)$, respectively.

With the definitions of the column vectors $\bar{\boldsymbol{y}}(s) = \boldsymbol{U}\,\bar{\boldsymbol{z}}(s)$ and $\bar{\boldsymbol{H}}(s) = \boldsymbol{U}\,\bar{\boldsymbol{F}}(s)$ where $\boldsymbol{U}$ is a unitary transformation that diagonalizes $\boldsymbol{A}$, Eq. B2 becomes a set of indexed equations,

$$\begin{aligned}\bar{y}_k(s) = {} & \frac{1}{s^2 + \gamma s + \Omega_k^2} \cdot \frac{\bar{H}_k(s)}{m} \\ & + \frac{s+\gamma}{s^2 + \gamma s + \Omega_k^2} \cdot y_k(0) + \frac{1}{s^2 + \gamma s + \Omega_k^2} \cdot \dot{y}_k(0),\end{aligned} \tag{B3}$$

where $\boldsymbol{y}(0) = \boldsymbol{U}\,\boldsymbol{z}(0)$ and $\dot{\boldsymbol{y}}(0) = \boldsymbol{U}\,\dot{\boldsymbol{z}}(0)$, k is the row index, and $\Omega_k = 2\omega\,\sin(\pi k/2N)$ is the kth element of the diagonalized matrix $\boldsymbol{U}^{\mathrm{T}}\boldsymbol{A}\boldsymbol{U}$. The two roots to the characteristic quadratic equation $\lambda^2 + \gamma\ \lambda + \Omega_k^2 = 0$ are λ_{1k}, $\lambda_{2k} = -\gamma\ /2 \pm i\Lambda_k$, where $\Lambda_k = \Omega_k\sqrt{1 - \left(\gamma^2/4\Omega_k^2\right)}$.

Consequently, Eq. B3 can be converted into the time domain by the inverse Laplace transform as follows:

$$y_k(t) = \frac{1}{m}\int_0^t d\tau\, H_{\boldsymbol{k}}(\tau)\left[e^{\lambda_{1k}(t-\tau)} - e^{\lambda_{2k}(t-\tau)}\right]/\left(\lambda_{1k} - \lambda_{2k}\right)$$
$$+ y_k(0)\left[\left(\lambda_{1k} + \gamma\right)e^{\lambda_{1k}t} - \left(\lambda_{2k} + \gamma\right)e^{\lambda_{2k}t}\right]/\left(\lambda_{1k} - \lambda_{2k}\right) \quad \text{(B4)}$$
$$+ \dot{y}_k(0)\left(e^{\lambda_{1k}t} - e^{\lambda_{2k}t}\right)/\left(\lambda_{1k} - \lambda_{2k}\right).$$

One can show that the unitary matrix $\boldsymbol{U}$ is simply a cosine Fourier transform (*33*). Hence,

$$z_n(t) = \sum_{k=0}^{N-1} y_k(t)\cos\left(\frac{k\pi}{N}\left(n + \frac{1}{2}\right)\right),$$
$$\dot{z}_n(t) = \sum_{k=0}^{N-1} \dot{y}_k(t)\cos\left(\frac{k\pi}{N}\left(n + \frac{1}{2}\right)\right), \quad \text{(B5)}$$
$$F_n(t) = \sum_{k=0}^{N-1} H_k(t)\cos\left(\frac{k\pi}{N}\left(n + \frac{1}{2}\right)\right),$$

and reversely,

$$y_0(0) = \frac{1}{N}\sum_{j=0}^{N-1} z_j(0), \quad y_k(0) = \frac{2}{N}\sum_{j=0}^{N-1} z_j(0)\cos\left(\frac{k\pi}{N}\left(j + \frac{1}{2}\right)\right),$$
$$\dot{y}_0(0) = \frac{1}{N}\sum_{j=0}^{N-1} \dot{z}_j(0), \quad \dot{y}_k(0) = \frac{2}{N}\sum_{j=0}^{N-1} \dot{z}_j(0)\cos\left(\frac{k\pi}{N}\left(j + \frac{1}{2}\right)\right), \quad \text{(B6)}$$
$$H_0(0) = \frac{1}{N}\sum_{j=0}^{N-1} F_j(0), \quad H_k(0) = \frac{2}{N}\sum_{j=0}^{N-1} F_j(0)\cos\left(\frac{k\pi}{N}\left(j + \frac{1}{2}\right)\right).$$

Therefore, by substituting Eq. B6 into Eq. B4 and then Eq. B5, with the values of λ_{1k} and λ_{2k}, Eq. 2 is readily obtained.

References:

1. M. T. Seidel, S. Chen, A. H. Zewail, *J. Phys. Chem. C* **111**, 4920 (2007).
2. J. H. Bechtel, *J. Appl. Phys.* **46**, 1585 (1975).
3. L. Jiang, H.-L. Tsai, *J. Heat Transfer* **127**, 1167 (2005).
4. S.-S. Wellershoff, J. Hohlfeld, J. Güdde, E. Matthias, *Appl. Phys. A* **69**, S99 (1999).
5. C. Thomsen, H. T. Grahn, H. J. Maris, J. Tauc, *Phys. Rev. B* **34**, 4129 (1986).

6. G. L. Eesley, B. M. Clemens, C. A. Paddock, *Appl. Phys. Lett.* **50**, 717 (1987).

7. O. B. Wright, K. Kawashima, *Phys. Rev. Lett.* **69**, 1668 (1992).

8. O. B. Wright, *Phys. Rev. B* **49**, 9985 (1994).

9. J. H. Hodak, A. Henglein, G. V. Hartland, *J. Phys. Chem. B* **104**, 9954 (2000).

10. M. Hase, K. Ishioka, J. Demsar, K. Ushida, M. Kitajima, *Phys. Rev. B* **71**, 184301 (2005).

11. C. Rossignol, J. M. Rampnoux, M. Perton, B. Audoin, S. Dilhaire, *Phys. Rev. Lett.* **94**, 166106 (2005).

12. G. V. Hartland, *Phys. Chem. Chem. Phys.* **6**, 5263 (2004).

13. G. V. Hartland, *J. Chem. Phys.* **116**, 8048 (2002).

14. G. V. Hartland, M. Hu, O. Wilson, P. Mulvaney, J. E. Sader, *J. Phys. Chem. B* **106**, 743 (2002).

15. S. D. Brorson, J. G. Fujimoto, E. P. Ippen, *Phys. Rev. Lett.* **59**, 1962 (1987).

16. C. K. Sun, F. Vallée, L. Acioli, E. P. Ippen, J. G. Fujimoto, *Phys. Rev. B* **48**, 12365 (1993).

17. J. Hohlfeld, J. G. Muller, S. S. Wellershoff, E. Matthias, *Appl. Phys. B* **64**, 387 (1997).

18. J. Chen, I. V. Tomov, H. E. Elsayed-Ali, P. M. Rentzepis, *Chem. Phys. Lett.* **419**, 374 (2006).

19. I. V. Tomov, P. Chen, P. M. Rentzepis, *J. Appl. Cryst.* **28**, 358 (1995).

20. C. Rose-Petruck *et al.*, *Nature* **398**, 310 (1999).

21. A. Cavalleri *et al.*, *Phys. Rev. Lett.* **85**, 586 (2000).

22. A. Plech *et al.*, *Europhys. Lett.* **61**, 762 (2003).

23. M. F. DeCamp *et al.*, *J. Synchrotron Radiat.* **12**, 177 (2005).

24. A. M. Lindenberg *et al.*, *Phys. Rev. Lett.* **84**, 111 (2000).

25. J. R. Dwyer *et al.*, *Philos. Trans. R. Soc. Ser. A* **364**, 741 (2006).

26. H. Park, X. Wang, S. Nie, R. Clinite, J. Cao, *Phys. Rev. B* **72**, 100301(R) (2005).

27. S. Nie, X. Wang, H. Park, R. Clinite, J. Cao, *Phys. Rev. Lett.* **96**, 025901 (2006).

28. E. Fermi, J. Pasta, S. Ulam, *LA*–1940 (1955).

29. J. M. Cowley, *Diffraction physics* (Elsevier, Amsterdam, 3rd ed., 1995).

30. *CRC handbook of chemistry and physics* (CRC Press, Boca Ration, FL, 1995), pp. E-43.

31. J. Hohlfeld *et al.*, *Chem. Phys.* **251**, 237 (2000).

32. C. Kittel, *Introduction to solid state physics* (Wiley, New York, 7th ed., 1996).

33. J. Tang, S. N. Dikshit, J. R. Norris, *J. Chem. Phys.* **103**, 2873 (1995).